UAV Photogrammetry-Based Leaf Area Index for Above-Ground Biomass Estimation in Wetlands

Regine Anne Faelga, Marco Assiri, and Sonia Silvestri

***Abstract*—Wetlands are highly productive and biologically diverse environments that provide numerous ecosystem services. Effective monitoring methods are critical to ensure their preservation and management. This article used UAV-derived RGB images and structure from motion (SfM) photogrammetry to create point clouds. Primary tie points were utilized as they are the more suitable representation of the raw 3-D information of the common features from the overlapping images. A leaf area index (LAI) estimation workflow for LiDAR was then tested on the UAV-SfM point cloud of two wetland types—alpine peatland and coastal salt marsh—to assess its applicability. The LAI and above-ground biomass (AGB) values for the peatland were 0.75–2.58 and 0–318.8 g/m^2, respectively, with R^2 of 0.67 and Pearson's coefficient of 0.82. For the salt marsh, the values range from 0.02 to 2.04 for the LAI and from 0 to 2378 g/m^2 for AGB, with R^2 of 0.84 and Pearson's coefficient of 0.86. Overall, the method is sensitive to vegetation density/biomass and works well in sparser and shorter vegetation as in the case of the salt marshes in the Mediterranean compared to densely vegetated wetlands, such as alpine peatlands. The flexibility and low-cost nature of UAV-SfM and its ability to produce quality information rapidly should be further maximized in vegetation monitoring and assessment even in other environments, such as agricultural lands and urban green spaces.**

***Index Terms*—Biomass, leaf area index (LAI), point clouds, structure from motion (SfM) photogrammetry, UAV, wetlands.**

I. Introduction

WETLANDS are ecosystems where the soil is covered or saturated by water throughout the year or at least during the vegetative season. Soil saturation influences soil development and the types of flora and fauna. There are fresh-, brackish-, and salt-water wetlands that develop either inland or along the coast and estuaries.

Received 19 December 2024; revised 29 March 2025; accepted 3 April 2025. Date of publication 8 April 2025; date of current version 9 June 2025. This work was supported in part by the University of Padova, STARS@UNIPD Programme, CHANGED—CHAracteriziNG pEatlands from Drones, in part by National Science Foundation, Coupled Ecological-Geomorphological Response of Coastal Wetlands to Environmental Change under Grant 2016068, and in part by the European Union National Recovery and Resilience Plan D.D. under Grant 1243 2/8/2022, Grant PE0000005. *(Corresponding author: Sonia Silvestri.)*

Regine Anne Faelga was with the Department of Land, Environment and Forestry, University of Padova, 35020 Padova, Italy. She is now with the Department of Biological, Geological, and Environmental Sciences, University of Bologna, 40126 Bologna, Italy (e-mail: reginefaelga@gmail.com).

Marco Assiri is with the Department of Land, Environment and Forestry, University of Padova, 35020 Padova, Italy (e-mail: marco.assiri@gmail.com).

Sonia Silvestri is with the Department of Biological, Geological, and Environmental Sciences, University of Bologna, 40126 Bologna, Italy (e-mail: sonia.silvestri5@unibo.it).

The R script, sample data, and additional information are included as supplementary materials in the Zenodo repository: 10.5281/zenodo.15162311.

Digital Object Identifier 10.1109/JSTARS.2025.3558893

Some important examples include peatlands, which act as a major global carbon (C) store, about 15–30% of the total world soil carbon pool accounting for more than 600-Pg carbon since the Last Glacial Maximum [1], [2], [3], [4], [5]. Despite covering only 3% of the earth's land surface, peatlands provide various ecosystem services that include biomass production for agricultural use, energy source, biodiversity support, recreation, climate, and water regulation as they can reduce flooding by slowing and absorbing rainwater and stabilize water composition by filtering runoff and metabolizing excess nutrients [6], [7], [8], [9]. Alpine peatlands, specifically those that are located in temperate regions such as the Italian Alps, support complex ecosystems composed of both fen and bog vegetation types with various taxa [10], [11], [12], as well as specialized endangered species and habitats; thus, these ecosystems are important to focus on [13], [14]. The combined temperature increases along with the summer precipitation decreases for temperate Europe could subject these ecosystems to groundwater level decrease, and peat mineralization increases with feedback release of greenhouse gases [6], [15], [16].

Another example is salt marshes, which serve as a transition zone between submerged and emerged environments occupying the intertidal landscape's upper margins [17]. Aside from their importance as carbon sinks (e.g., blue carbon), these vital ecosystems offer valuable services such as coastal protection from erosion through sediment stabilization and wave action buffering [7], nursery areas for coastal biota, and filtering of nutrients and pollutants [17], [18], [19]. Similar to other wetland types, these valuable coastal ecosystems are at risk of possible irreversible impacts due to climate changes and human interference [20].

Alpine peatlands and salt marshes are characterized by short vegetation that often grows on flooded surfaces—the former due to ponds and the latter from tides. Alpine peatlands have highly complex and heterogeneous herbaceous vegetation covers that are usually very dense. On the other hand, salt marshes have halophytic vegetation species (i.e., macrophytes) that are typically organized in characteristic patches [21], [22] and are also usually very dense, even though in the Mediterranean salt marshes, they are not as dense compared to those in the U.S. and China. Effective monitoring methods are necessary to address the loss of these valuable ecosystems. At the same time, accurate knowledge of wetland processes is important to maximize preservation and management effectiveness [23].

Above-ground biomass (AGB) serves as an indicator of ecosystem health, resilience, and carbon storage [24], [25], [26].

Ground-measured AGB is considered one of the most accurate ways, but this method tends to be invasive and limited as it can destroy vegetation and cannot provide an estimation at a large scale. In alpine peatlands and salt marshes, ground-based AGB measurements are challenging due to limited accessibility and the complexity of vegetation cover and dynamics [10], [11], [12], [27], [28], [29], [30], [31]. Over the years, remote sensing technology has been increasingly used as a complementary tool for wetland AGB estimation. However, key limitations remain—the availability of data and algorithms capable of enabling studies at very high to ultrahigh spatial resolution, which are essential for understanding vegetation properties and associated biogeochemical processes [10], [29], [32], [33], [34].

Among the several approaches to estimate AGB and other biophysical parameters at ultrahigh spatial resolution, the most promising are based on UAV-derived 3-D point clouds. Structural features, such as vegetation height, improve the accuracy of vegetation classification [35], [36], [37], especially when deep learning approaches are considered [38]. Vegetation height has been used to estimate AGB in homogeneous vegetation types, such as grasslands [39] and crop fields [40] [41], [42]. However, in areas covered by a variety of species or vegetation communities, vegetation height may not correlate well with AGB. This highlights the need to better exploit the full range of metrics that can be derived from 3-D point clouds for AGB estimation.

New possibilities are now available through computer vision, where UAV point clouds are used for environmental reconstructions, digital twins, and landscape planning scenarios [43], [44]. In this work, we apply to wetland vegetation a methodology that was originally developed for forested areas using airborne LiDAR [45]. Through the gap probability, this approach retrieves an estimate of the leaf area index (LAI), which is defined as one-half of the total green leaf area per unit of the horizontal ground surface and is a vital vegetation parameter that has been broadly utilized in growth estimation studies and as an AGB proxy [10], [33], [46], [47]. The LAI estimated through gap fraction is a powerful descriptor of the canopy structure [48], [49]. Therefore, it is a key biophysical variable used in modeling plant growth [50], photosynthesis [51], transpiration [52], and nutrient cycling [53]. Like AGB, field LAI measurements give the highest accuracy but are impractical and unfeasible in terms of spatial repeatability over difficult-to-reach areas, such as wetlands.

Some studies have already utilized 3-D point clouds from LiDAR—both airborne and UAV-based on wetland ecosystems for LAI estimation [10], [54]. However, the number of studies on LAI estimation based on the use of 3-D point clouds from UAV photogrammetry is limited [23], [55], [56]. Structure from motion (SfM) photogrammetry is an affordable alternative to acquire point clouds that reconstruct 3-D point clouds by overlapping multiple 2-D images using the distances calculated between the image key points [23], [55], [56], [57]. However, previous applications to densely vegetated salt marsh systems have failed to provide accurate results in determining vegetation characteristics [23]. In this study, we investigate the reasons for this failure, hypothesizing that it is related to vegetation type and percentage cover. We speculate that when vegetation cover is low, as is typically the case in European salt marshes, point clouds from UAV photogrammetry can be successfully used to estimate the LAI and, therefore, AGB. This study primarily focused on developing a simple workflow for processing UAV-derived RGB images using SfM photogrammetry to generate RGB point cloud data replicating the 3-D structure of LiDAR. Primary tie points were used instead of the derived dense point clouds to estimate the LAI through the gap probability model [45] and, finally, AGB. In SfM, primary tie points are obtained by matching distinct features across several overlapping images, resulting in a sparse but highly accurate point cloud that forms the basis of the 3-D reconstruction. In contrast, the dense point clouds are generated during the densification phase and, while they provide greater spatial detail, they are generally less geometrically reliable than primary tie points. The applicability and effectiveness of the established workflow were tested using data collected from two wetlands: one with high vegetation cover, an alpine peatland in the Italian Alps, and other with typically low vegetation cover, a salt marsh along the Adriatic Sea coast.

Section II provides information on the selected study sites. It also discusses the field and drone data collection, the established methodological framework, and the parameter values applied. The succeeding section is about the model validation and AGB estimation results, followed by a discussion and conclusions. The R script, sample data, and additional information are included as supplementary material.

II. Materials and Methods

A. Study Site Characterization

The two wetlands in this study are both located in the Veneto region, northeastern Italy, as shown in Fig. 1. The selected alpine peatland has an area of 130 000 m^2 and is located in the municipality of Danta di Cadore in Belluno province at an altitude between 1358 and 1425 m relative to mean sea level (m.s.l.). The selected salt marsh area is part of the 470 000-m^2 San Felice marsh located in the northeastern part of the Venice Lagoon.

Plant species of the Danta peatland are grouped into three phytosociological alliances [10], [58]. Species with plant heights between 0.1 and 0.9 m attributed to the alliance *Caricion davallinae* Klika 1934 or typical of fen community are present (e.g., *Schoenus ferrugineus L.*, *Trichophorum alpinum (L.)* Pers., *Trichophorum cespitosum (L.)* Hartm., *Eriophorum latifolium* Hoppe, *Tofieldia calyculata (L.)* Wahlenb, *Rhynchospora alba (L.)* Vahl, *Drosera anglica Huds.*, and *Sphagnum majus (Russ.)* C. Jens) are also present, along with species of typically raised bog communities, such as *Sphagnum magellanicum* Brid., *Eriophorum vaginatum L.*, *Andromeda polifolia L.*, *Calluna vulgaris (L.)* Hull, *Vaccinium spp.*, or *Pinus mugo* Turra. The presence of *Phragmites australis (Cav.)* Trin. Ex Steud species is also observed, as shown in Fig. 1, with a maximum height that ranges from 66 to 127 cm. The terms "bog" and "fen" are linked to ombrotrophic (i.e., fed by rain) and minerotrophic (i.e., fed by groundwater) typical vegetations as used in the "Habitats Directive" (DIR 92/43/CEE) [10].

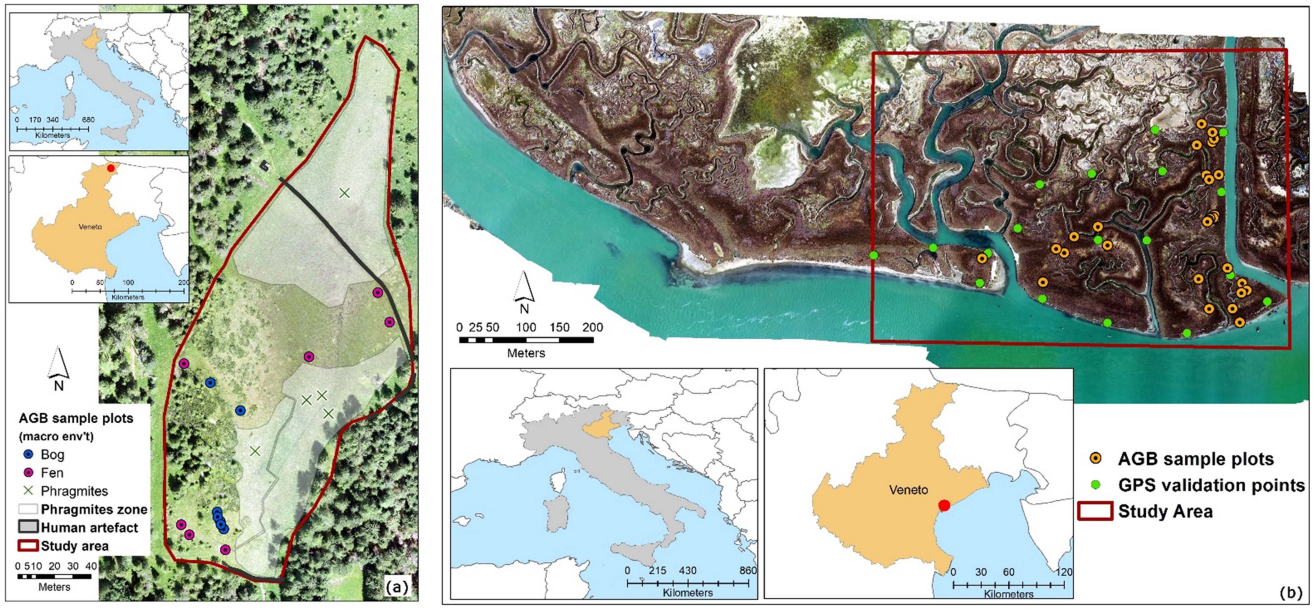

Fig. 1. Study site maps of the alpine peatland in (a) Danta di Cadore in Belluno, Italy, and (b) San Felice salt marsh in the Venice Lagoon, Italy.

The halophytic species present in the San Felice salt marsh are *Limonium narbonense*, *Sarcocornia fruticosa*, *Juncus maritimus*, *Salicornia veneta*, *Pucinellia palustris*, *Inula crithmoides*, *Spartina maritima*, and *Spartina anglica* [29]. These species are closely correlated to elevation and local geomorphologic characteristics [21], [28], [29], [59], [60], [61].

B. Field and UAV Data Collection

The field survey for the Danta peatland was performed in July 2021. For the vegetation sampling and AGB measurements, there are 18 sampling sites representing the vegetation alliance or morphotypes in the area. The field sampling was performed using a 0.5 m $\times$ 0.5 m quadrat, wherein vegetation cover, vegetation height, and AGB were measured. A Topcon Hyper V GNSS system (0.010 m of horizontal accuracy and 0.015 m of vertical accuracy in real-time kinematic (RTK) mode) was used to geolocate the sampling sites. Topographic points were also collected along the human artifacts in the area (boardwalk) as validation data for the digital elevation model (DEM). The UAV flight survey for the Danta peatland was on 23 July 2021, with the survey specifications listed in Table I.

The vegetation sampling and validation points collection for the San Felice salt marsh were also performed alongside the drone flight survey on 5–11 September 2021. A total of 36 AGB measurements and 113 topographic control points were selected and geolocated using Leica Viva GNSS GS15 RTK GPS, 24 of which are the drone ground control points (GCPs). The complete UAV flight survey and camera specifications are summarized in Table I. Both UAV flight surveys have geodetic vertical units in meters relative to m.s.l., and the coordinate system used was WGS84 Zone 33N.

C. Methodological Framework

1) SfM Workflow: The methodological framework of this study encompasses four main processes (see Fig. 2). The raw image files from the UAV surveys were subjected to SfM processing using Agisoft Metashape Professional version 2.

A total of 434 RGB frames for the Danta peatland and 665 for the San Felice salt marsh were collected in the automatic shooting mode with a frontal and lateral overlap of 80%. An initial quality assessment was then performed, wherein only images with a quality value of $>$0.50 units based on the sharpness level were retained. The images were then aligned at high or highest, depending on the data size and processing capacity of the workstation. Higher accuracy settings help to obtain more accurate camera position estimates [62]. Other alignment parameters were set, such as generic preselection, reference preselection, key, and tie point limit, options for exclusion of stationary points, guided image matching, and adaptive camera model fitting. Given the data size difference and hardware limitation, the accuracy level for the Danta peatland was set to the highest, while the San Felice salt marsh was set at high. The rest of the values applied for each parameter are indicated in Table II.

Once the tie points were created, the reference settings were adjusted depending on the coordinate system used for the camera and GCP. The coordinate system was set to WGS 84 Zone 33N for both surveys. Images were then georeferenced using the topographic point measurements. Each GCP was assigned as either a control point that was used to reference the model or a checkpoint to validate the camera alignment accuracy and optimization procedure results [62]. The Danta peatland had five control and two checkpoints, while the San Felice salt marsh had 17 control and seven checkpoints. Once all the images with known GCP were georeferenced, initial optimization was applied using the selected parameters in Table II.

TABLE I
UAV FLIGHT SURVEY SPECIFICATION FOR THE TWO STUDY SITES

Parameters	Danta peatland	San Felice salt marsh
Drone model	DJI Matrix 300 RTK	DJI Matrix 300 RTK
Flying height (Above Ground Level)	100 m	100 m
Velocity	5 m/s	5 m/s
Lateral overlap	80%	80%
Frontal overlap	80%	80%
Camera parameters	DJI Zenmuse L1 with 1" CMOS camera Effective Pixels: 20 MP	DJI Zenmuse L1 with 1'' CMOS camera Effective Pixels: 20 MP
Shooting mode	Automatic	Automatic
Focal length	8.8/24 mm (equivalent)	8.8/24 mm (equivalent)
Aperture range	f/2.8 – f/11	f/2.8 – f/11
Number of bands	3	3
Number of control points	7	24
Projected coordinate system	WGS 1984 UTM 33N	WGS 1984 UTM 33N
Number of RGB	434	665
frames		

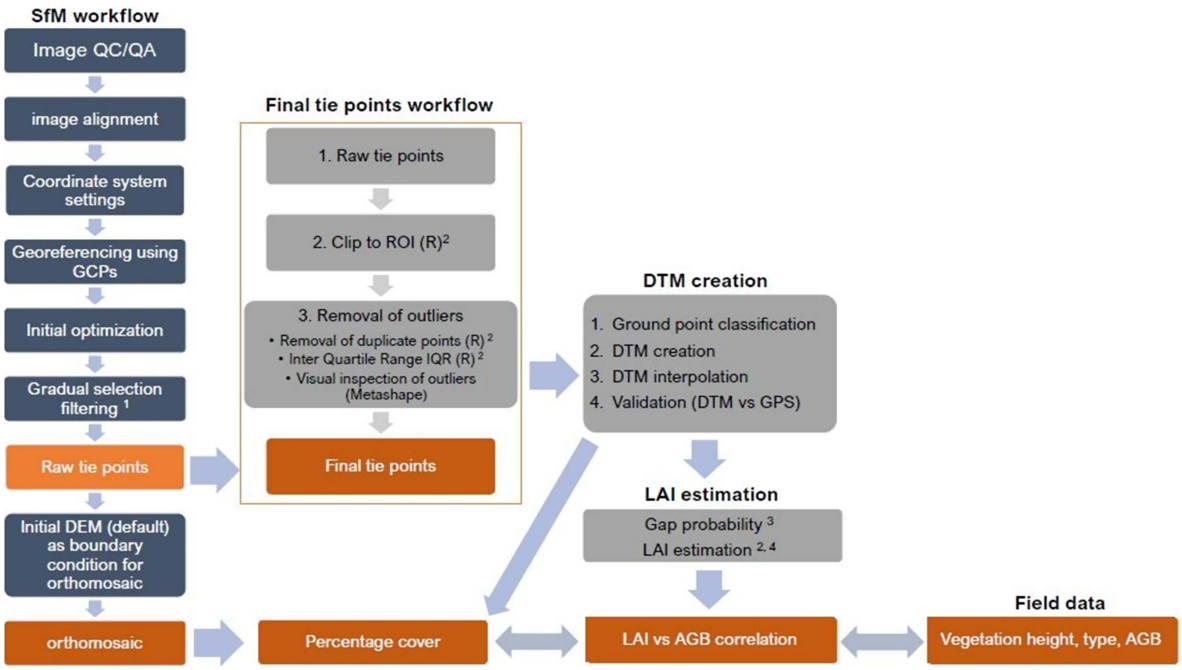

Fig. 2. Methodological framework. The gradual selection filtering was based on Over et al. [63] (1). The LAI estimation process and gap probability equation were based on Assiri et al. [10] (2), Richardson et al. [45] (3), and Lalimi et al. [66] (4).

Since the goal was to obtain the raw 3-D information from SfM, the primary tie points were more suitable for the needs of this study than the dense point clouds. The gradual selection filtering workflow, adapted from [63], was implemented to reduce error by selecting and removing low-quality tie points and iterating optimization. The quality metrics used in this step were based on the camera geometry of the images. Poor geometric relations between cameras were selected in reconstruction uncertainty, while the reprojection accuracy parameter selected tie points with poor matching accuracies. Finally, tie points that

TABLE II
SUMMARY OF THE PARAMETER VALUES APPLIED IN EACH STEP OF THE METHODOLOGICAL FRAMEWORK

Workflow parameter	Danta peatland 2021 (area = 24 000 m^2)	San Felice salt marsh 2021 (area = 470 000 m^2)	Remarks
SfM tie point alignment accuracy	Highest	High	Higher accuracy settings help to obtain more accurate camera position estimates. 1) High accuracy setting the software works with the photos of the original size. 2) Highest accuracy setting upscales the image by a factor of 4. Since tie point positions are estimated based on feature spots found on the source images, it may be meaningful to upscale a source photo to accurately localize a tie point.
Generic preselection	Yes	Yes	The mode of the overlapping pairs of photos is selected by matching photos using lower accuracy first.
Reference preselection	Source	Source	In the source preselection mode, the overlapping pairs of photos are selected based on the measured camera locations (if present).
Key point limit	40 000	40 000	Indicates the upper limit of feature points on every image to be considered during current processing. Using a 0 value allows us to find as many key points as possible but may result in producing less reliable points.
Tie point limit:	0	0	The upper limit of matching points for every image.
Exclude stationary tie points	Yes	Yes	Excludes tie points that remain stationary across multiple different images.
Guided image matching	Yes	Yes	Using this parameter can improve results for images with vegetation.
Adaptive camera model fitting	No	No	Enables automatic selection of camera parameters to be included in adjustments based on their reliability estimates.
Initial camera optimization alignment parameters	Fit f, Fit k1, Fit k2, Fit k3, Fit cx,cy, Fit p1, Fit p2, and adaptive camera model fitting applied	Fit f, Fit k1, Fit k2, Fit k3, Fit cx,cy, Fit p1, Fit p2, and adaptive camera model fitting applied	Default camera optimization parameters applied by Agisoft Metashape. The adaptive camera model fitting option enables the automatic selection of camera interior orientation parameters to be adjusted.
SfM gradual selection parameters 1. Filtering by Reconstruction Uncertainty = 10 2. Filtering by Projection accuracy = 3 3. Filtering by Reprojection error = 0.3 pixels	The same parameters were applied. Final number of points: 1,729,335 RMS reprojection error = 0.15 (0.24 pixels)	The same parameters were applied. Final number of points: 3,564,291 RMS reprojection error = 0.14 (0.31 pixels)	Target RMSE reprojection is 0.18 pixels
***R* processing** 1. Clipped to AOI 2. 50cm grid resolution 3. Noise cleaning: IQR 4. Ground classification: PMF 6. LAI estimation	The same parameters were applied as in [10] + additional editing in Agisoft Metashape + interpolation of DTM in QGIS.	The same parameters were applied as in [10] + additional editing in Agisoft Metashape +interpolation of DTM in QGIS	Additional editing in Agisoft metashape in terms of the following: 1. Removal of additional noise that was not removed during the IQR process. 2. Reclassifying point cloud that is validated as ground (for bare areas) DTM interpolation was performed in QGIS using the GDAL fillnodata tool (IDW at 1pixel search window)
GIS processing **1.** Vectorization of the LAI csv **2.** DTM validation **3.** Clipping of selected cells for LAI versus AGB correlation and point density	+interpolation of DTM that is used as input in the LAI estimation	+ interpolation of the DTM that is used as input in the LAI estimation	For the DTM validation: 1. Danta: offset of +0.32m was applied to the final DTM values to be compared. 2. San Felice: no offset value was applied.
***R*/Python/MS Excel** 1. Correlation and significance testing	Same processing	Same processing	

were the result of false matches were selected in the reprojection error parameter. The detailed values of the parameters applied, the final RMS reprojection error in pixels, and the final number of tie points are given in Table II.

2) Final Tie Point Workflow: The tie point data from the previous step were then used as input for the second phase of the methodology based on the established workflow of [10], wherein the "lidR" package [64] in the R environment (v.4.2.2) was utilized. Tie points were clipped to region of interest (ROI); then, duplicate points and noise were removed. The inter quartile range (IQR) was used in the initial noise removal. In case of outliers not removed in the IQR process, additional deletion was performed in Agisoft Metashape Professional.

3) Digital Terrain Model Creation and Validation: The digital terrain model (DTM) creation also follows the established methodology of [10] with an additional process applied. In this phase, the initial step is to classify ground points using the progressive morphological filter (PMF) of [65] with incremental window size (0.25, 0.50, 2, 5, and 10 m) and elevation thresholds (0.02, 0.05, 0.50, 1.5, and 3.5). The result from the PMF was used to create the DTM by assigning to each 0.5-m resolution grid cell the lowest elevation value of the ground points falling therein [10], [66]. The method was applied to increase the probability of selecting an elevation value that reaches the ground. Grid cells in the DTM raster that have no data were interpolated by calculating the surrounding pixel values (1-pixel window size) using inverse distance weighting (IDW). The IDW interpolation was performed in QGIS 3.22.4 using the algorithm derived from the Geospatial Data Abstraction Library (GDAL) [67]. This method was used since the DTM raster for the San Felice salt marsh produced salt-and-pepper-like terrain, and some of the ground validation points had no data. The same interpolation parameters were applied to the Danta peatland to ensure data comparability between the two wetlands. The vertical accuracy of the DTMs was assessed by comparing the DTM values and the measured ground validation points on flat surfaces (the boardwalk for Danta and the 18 drone control points for San Felice) using scatterplot, R^2, Pearson's correlation coefficient, standard error (SE), and mean absolute error (MAE). The DTM values on vegetated zones and transects with available GPS data in both wetlands were also utilized to validate the model's performance in vegetated areas.

4) LAI Estimation: The LAI estimation process in this research used the gap probability approach, i.e., the probability that a laser beam penetrated the canopy to reach the ground [10], [42], [45], [68]

$$P\ (\theta) = \exp\left(\frac{-G\,(\theta)\,\mathrm{LAI}}{\cos\theta}\right) \tag{1}$$

where θ is the view zenith angle, and $G(\theta)$ defines the leaf clumping and the mean leaf projection in the direction θ. $G(\theta)$ varies between 0 and 1

$$\mathrm{LAI} = -\frac{\cos\,(\theta)}{k} * \ln\left(\frac{Rg}{Rt}\right) \approx -\frac{1}{0.5} * \ln\left(\frac{Rg}{Rt}\right) \tag{2}$$

where k is the extinction coefficient, Rg is the ground-classified points, and Rt is the total number of points.

In this work, we assume that instead of the LiDAR point cloud, the RGB tie points can be used in the equations. The hypothesis made on the view zenith is analogous because the RGB images are collected at the nadir and photograms are highly overlapped. Once the RGB tie points are gridded, $P(\theta)$ can be approximated for each grid cell using the fraction of ground-classified points (Rg) to the total number of points in that cell (Rt). The LAI was computed by using the inverted formula of (1) and (2), with the assumption that 1) the leaf angle distribution is spherical; therefore, $k \approx 0.5$, and 2) θ values are small, so $\theta \approx 0$.

Similar to [10], the direct use of the number of ground points to calculate the LAI using (2) was also not implemented due to the large vertical variability of the ground-classified points on vegetated areas compared to flat reference surfaces. As an alternative, the RGB tie points were considered to be generated by ground reflections if the height, relative to the local ground elevation at a particular DTM cell value, was below a fixed threshold set at 5 cm [10], [66].

The inputs for the LAI estimation are the final RGB tie points, DTM raster, grid cells raster, and scan angle raster. The output is a comma-separated value (.csv) file that is processed in a GIS software environment to produce the final LAI map. Similar to previous approaches where LAI field observations were not available [10], [66], [69], the accuracy of the results was directly assessed using the AGB observations and the vegetation percentage cover, as described in the next sections.

5) Accuracy Verification: Field observations of the AGB were used to verify the method's accuracy. For each sampling location, strategically located within homogeneous vegetation patches, the UAV-derived LAI values were calculated as arithmetic averages from 20 selected 0.5-m cells, identified through expert analysis of orthophotos, and located near each sampling site, while ensuring that cells affected by sampling disturbance were excluded. Three sets of 20 cells on bare artificial and ground surfaces (with AGB $= 0$) were also included to improve the dataset and the linear regression between the LAI variables and the AGB values. The coefficient of determination (R^2) was used to evaluate the strength of the relationship between the observed AGB and the UAV-derived LAI. In addition, the p-value was calculated to assess the statistical significance of the model, providing a measure of the evidence against the null hypothesis.

6) Point Density and Percentage Cover: Point density and the proportion of points reaching the ground were evaluated to assess how the method's effectiveness depends on vegetation cover, which varies within each wetland and, more significantly, between the two different wetland types. An orthophoto-based selection of 20 grid cells (0.5 m $\times$ 0.5 m) per sample plot was performed. In this case, the selected grid cells included a varied mix of ground and vegetated areas, and were not necessarily located close to the field sampling sites. The percentage of tie points classified as ground or vegetation was then calculated accordingly. To verify whether these percentages reflect the actual variation in vegetation percentage cover, a statistical approach [70] based on visual inspection was adopted. The method is similar to a classic visual ecological survey performed in the field. However, orthophotos were used in this case assuming that the operator has a clear overview of the area and can

properly distinguish ground versus vegetated pixels [71]. The method's accuracy, therefore, depends on the image quality and the operator's expertise. For the percentage cover analysis, the visual inspection was done on points regularly spaced on a grid of 0.25 m × 0.25 m using the previously selected 0.5 m × 0.5 m grid cells as their boundary condition. A finer resolution grid was used to create the points to ensure that the cover variability could be accounted for. The cover is determined by the operator if the tie point will fall on either ground or vegetation, and then, the percentage calculations between ground and vegetation points were done to quantify the percent cover. The orthophotos have a pixel size of 0.023 m × 0.023 m for Danta, and 0.028 m × 0.028 m for San Felice.

III. Results

A. SFM Processing

Figs. 3 and 4 show the RGB tie point cloud processing results of the Danta peatland and the San Felice salt marsh. After the gradual selection filtering, the total RGB tie point data are 1 729 335 and 3 564 291. The total root-mean-squared error (RMSE) values of the control point and the checkpoint of the Danta peatland are 0.016 and 0.045 m, respectively, while 0.016 and 0.026 m are the values for the San Felice salt marsh.

After clipping to ROI and noise removal, the RGB tie point cloud was further reduced to 1 027 754 points (22.73 points/m^2) for the Danta peatland and 1 858 344 points (8.53 points/m^2) for the San Felice salt marsh. The PMF ground filtering result shows the difference between the vegetation densities of the two wetlands. The nonground points of the Danta peatland are so dense that the detected ground points are hardly visible [see Fig. 3(d)], while in the San Felice salt marsh, the vegetation is sparser, so ground points are visible [see Fig. 4(d)]. The point density and percent cover assessment in Table III and Fig. 5 further reveal that most of the tie points could not reach the ground in the Danta peatland compared to the San Felice salt marsh. The ground classification method worked well in San Felice, showing a good correlation between the percentage cover and point density ($R^2 = 0.72$) compared to the correlation observed in Danta with an R^2 of 0.17 (see Figs. 8 and 9 in the Appendix).

For elevation values, the Danta peatland has values from 1395.78 to 1420.94 m, while the San Felice salt marsh has values from –2.44 to 0.97 m.

B. Significance Testing for the Interpolated DTM

Regression statistics for both wetlands were performed to determine the statistical significance of implementing the IDW interpolation on the DTM processing (see Table IV). This is to determine if the p-value improves or at least is stable after the interpolation process. The data used in this test are from the boardwalk points in Danta and the 18 drone control points within the ROI in San Felice, since these points represent ground surfaces. There was not much significant change in terms of the R^2 and p-values for Danta peatland, but sample points with data have increased from 164 to 175. The R^2 for the interpolated DTM of the San Felice salt marsh has a slightly lower value than the data without interpolation. Still, significant improvement in the p-value and the number of samples with data (from 9 to 18) was evident. Hence, the use of IDW interpolation was considered valuable for the validation process of the DTMs.

C. DTM Validation

The Danta peatland has a total of 175 ground validation points along the boardwalk (see Fig. 10 in the Appendix). Plotting the elevation value of the DTM and GPS, a mean difference of +0.32 m is apparent, which might have been due to datum shifting between the drone and ground GPS. The data used in the DTM validation for the Danta peatland included the 0.32-m mean difference as an offset (see Fig. 11 in the Appendix). There is a good correlation between the DTM and GPS elevation values with R^2 of 0.89 and Pearson's coefficient at 0.94 along the boardwalk. However, if the ground elevation values on the vegetation zones are considered, a significant MAE of 0.17–0.28 m was observed [see Table V(a)].

The validation data used for the San Felice salt marsh are the 18 GCP points within the selected ROI (ground surfaces) and 11 transects (vegetated surfaces) (see Fig. 12 in the Appendix). There is no evident shift between the GPS and DTM elevation values, so no offset was applied before the correlation analysis (see Fig. 13 in the Appendix). The correlation between the DTM and GPS elevation values of the GCPs has an R^2 of 0.62 and Pearson's coefficient of 0.79, with 0.06-m SE and 0.05-m MAE. The overall SE and MAE values in the vegetated areas in the salt marsh are much lower than in the Danta peatland, with SE values ranging from 0.02 to 0.06 m and MAE values from 0.07 to 0.15 m [see Table V(b)].

D. LAI and AGB Estimation

The estimated LAI of the Danta peatland ranges between 0 and 7.05 [see Fig. 6(a)]. Out of the 18 sampling sites, only bogs and fens (12 plots) were considered in the LAI and AGB correlation. Phragmites (six plots) were excluded from the analysis since the RGB tie points produced high distribution variability within these sampling plots. Phragmites have tall and dense characteristics that make them prone to being affected by wind and pose a difficulty in obtaining sufficient and representative tie points in the SfM processing. The LAI and AGB values range from 0.75 to 2.58 and from 0 (for control plots) to 318.8 g/m^2, respectively, with R^2 of 0.67 and Pearson's coefficient of 0.82.

The estimated LAI ranges from 0 to 5.78 for the San Felice salt marsh [see Fig. 6(b)]. The correlation contains 32 sampling points—including control plots, with LAI values ranging from 0.02 to 2.04 and AGB values ranging from 0 to 2378 g/m^2, with R^2 of 0.84 and Pearson's coefficient of 0.86. The estimated AGB distribution map across the San Felice marsh for 2021 using the correlation equation is shown in Fig. 7.

IV. Discussion

A. SfM Processing

UAV-SfM point clouds from RGB images have already been used in several vegetation mapping and monitoring studies, but to our knowledge, this is the first one to explore primary tie

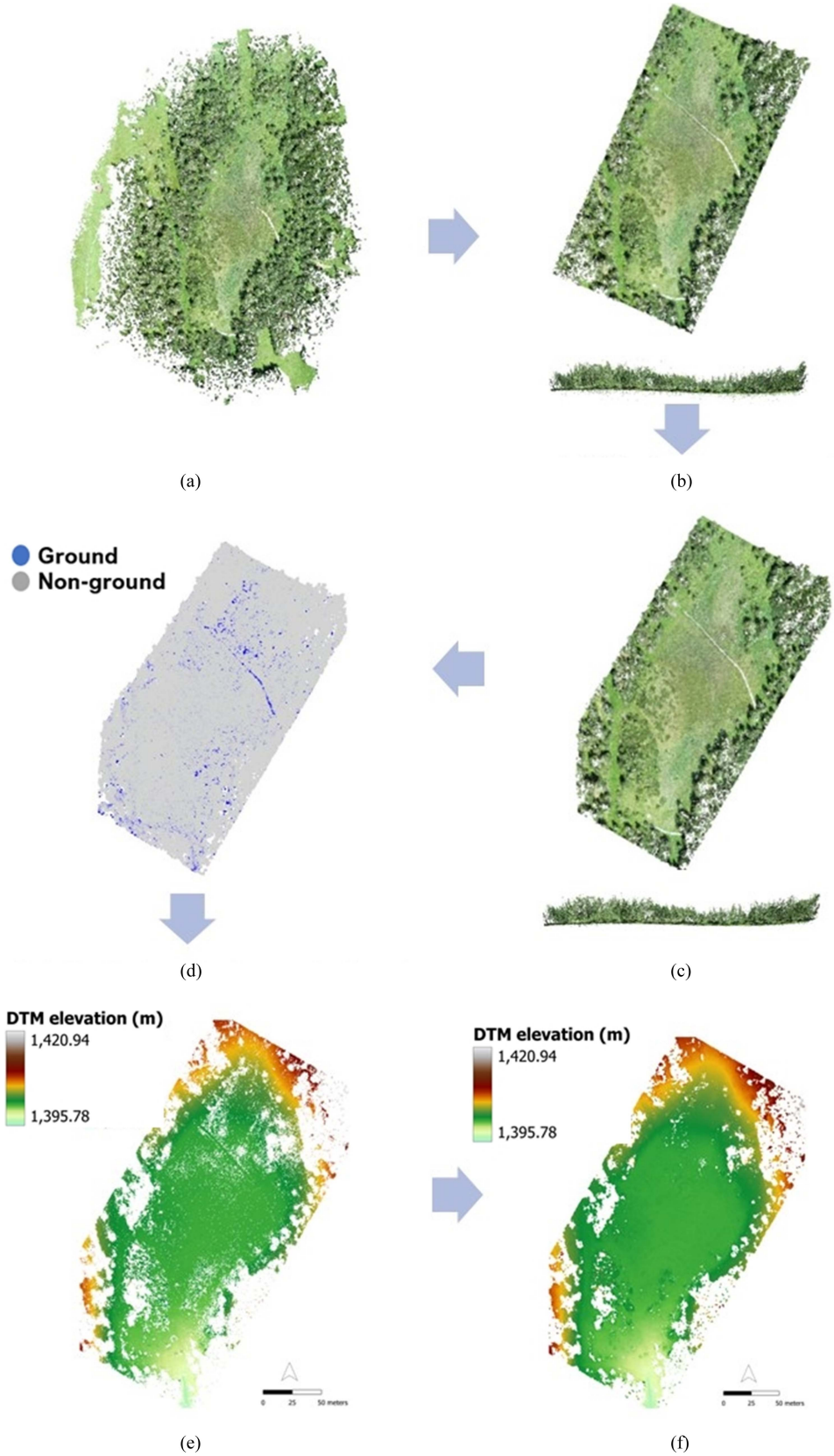

Fig. 3. RGB point cloud processing of the Danta peatland 2021. (a) Raw tie point (gradual selection applied). (b) Clipped to ROI. (c) Noise removed (IQR). (d) Ground classified (PMF). (e) DTM (no interpolation) (lowest point at 50-cm grid). (f) DTM interpolated (IDW, 1-pixel window).

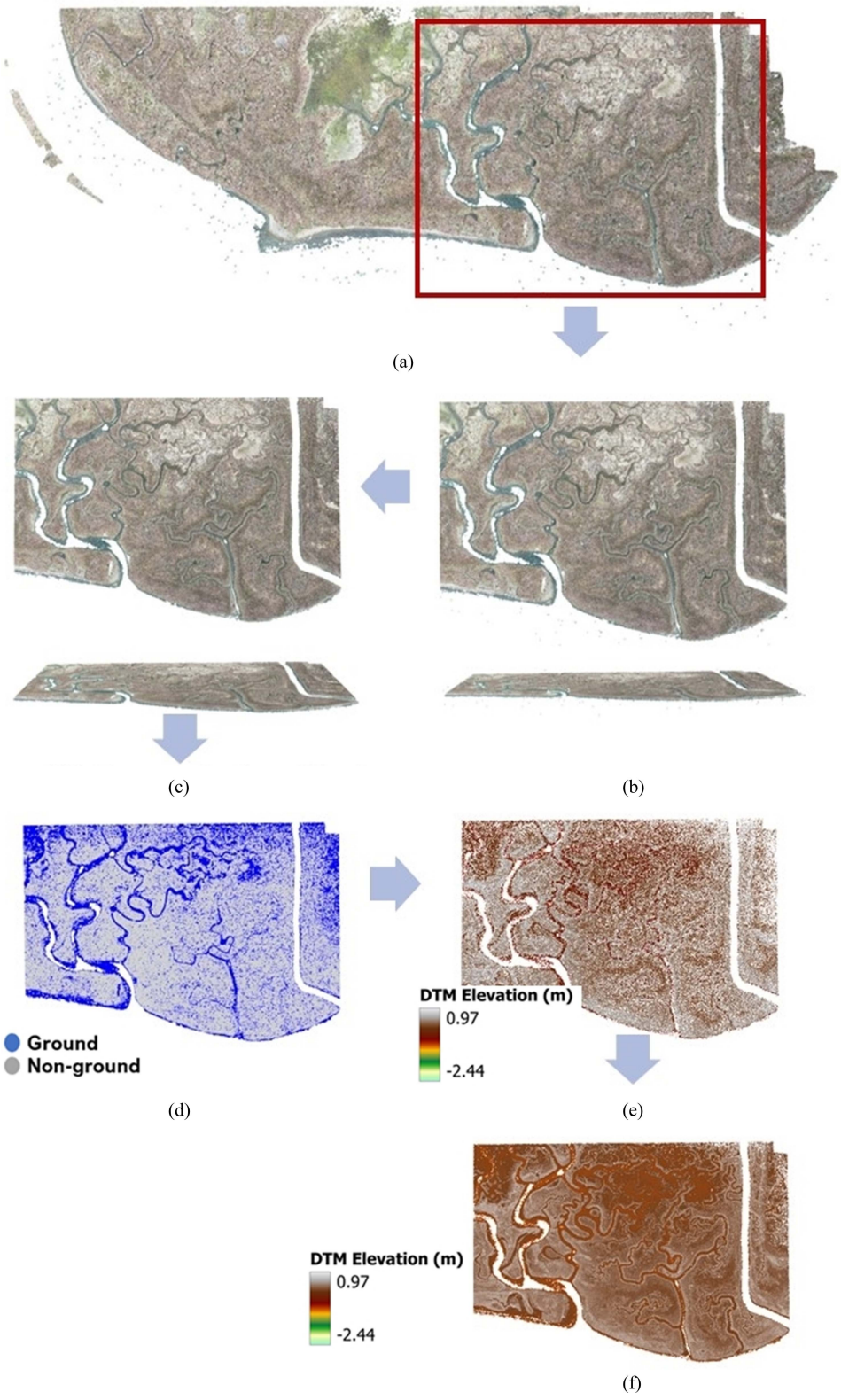

Fig. 4. RGB point cloud processing of the San Felice salt marsh 2021. (a) Raw tie point (gradual selection applied). (b) Clipped to ROI. (c) Noise removed (IQR). (d) Ground classified (PMF). (e) DTM (no interpolation) (lowest point at 50-cm grid). (f) DTM interpolated (IDW, 1-pixel window).

TABLE III
POINT DENSITY AND PERCENT COVER ASSESSMENT FOR THE DANTA PEATLAND AND THE SAN FELICE SALT MARSH

DANTA PEATLAND	**Point density (tie points)**					**Percent cover (orthophoto based)**				
Plot	**Ground points (*Rg*)**	**Vegetation points (*Rv*)**	**Total points (*Rt*)**	**Ground % (PD *Rg* %)**	**Vegetation % (PD *Rv*%)**	**Ground points (*Rg*)**	**Vegetation points (*Rv*)**	**Total points (*Rt*)**	**Ground (PC *Rg* %)**	**Vegetated (PC *Rv*%)**
Danta_1A	81	168	249	32.53	67.47	5	109	114	4.39	95.61
Danta_1B	104	122	226	46.02	53.98	3	107	110	2.73	97.27
Danta_1C	102	162	264	38.64	61.36	2	119	121	1.65	98.35
Danta_1D	102	154	256	39.84	60.16	3	106	109	2.75	97.25
Danta_2A	111	177	288	38.54	61.46	5	105	110	4.55	95.45
Danta_2B	73	148	221	33.03	66.97	3	128	131	2.29	97.71
Danta_2C	114	174	288	39.58	60.42	7	106	113	6.19	93.81
Danta_4A	94	157	251	37.45	62.55	4	122	126	3.17	96.83
Danta_4B	70	154	224	31.25	68.75	0	113	113	0	100
Danta_4C	85	173	258	32.95	67.05	1	117	118	0.85	99.15
Danta_5A	114	165	279	40.86	59.14	7	125	132	5.30	94.70
Danta_5B	81	139	220	36.82	63.18	1	132	133	0.752	99.25
SAN FELICE SALT MARSH	**Point density (tie points)**					**Percent cover (orthophoto based)**				
Plot	**Ground points (*Rg*)**	**Vegetation points (*Rv*)**	**Total points (*Rt*)**	**Ground % (PD *Rg* %)**	**Vegetation % (PD *Rv*%)**	**Ground points (*Rg*)**	**Vegetation points (*Rv*)**	**Total points (*Rt*)**	**Ground (PC *Rg* %)**	**Vegetated (PC *Rv*%)**
SF1	55	1	56	98.21	1.79	99	0	99	100.00	0.00
SF2	43	2	45	95.56	4.44	99	0	99	100.00	0.00
SF3	25	6	31	80.65	19.35	89	10	99	89.90	10.10
SF4	13	2	15	86.67	13.33	67	32	99	67.68	32.32
SF5	28	8	36	77.78	22.22	60	39	99	60.61	39.39
SF6	10	5	15	66.67	33.33	65	34	99	65.66	34.34
SF7	22	11	33	66.67	33.33	77	22	99	77.78	22.22
SF8	26	15	41	63.41	36.59	62	37	99	62.63	37.37
SF9	23	4	27	85.19	14.81	76	23	99	76.77	23.23
SF10	26	25	51	50.98	49.02	44	55	99	44.44	55.56
SF11	34	23	57	59.65	40.35	45	54	99	45.45	54.55
SF12	14	3	17	82.35	17.65	78	21	99	78.79	21.21

TABLE IV
REGRESSION STATISTICS TO COMPARE THE STATISTICAL SIGNIFICANCE OF USING DTM INTERPOLATED DATA

	Danta peatland (no interpolation)	**Danta peatland (IDW interpolated)**	**San Felice salt marsh (no interpolation)**	**San Felice salt marsh (IDW interpolated)**
Regression Parameters				
Multiple *R*	0.94	0.94	0.82	0.79
R^2	0.89	0.89	0.67	0.62
Adjusted R^2	0.89	0.89	0.62	0.60
SE	0.06	0.05	0.06	0.06
Observations	164	175	9	18
ANOVA				
df	1	1	1	1
SS	4.19	4.28	0.05	0.11
MS	4.19	4.28	0.05	0.11
F-stat	1342.95	14222.689	14.11	26.41
Significance *F* (*p*-value)	**2.58E-8**	**2.20231E-8**	**0.007105**	**9.8884E-05**

df: degrees of freedom; SS: sum of square; MS: mean square.

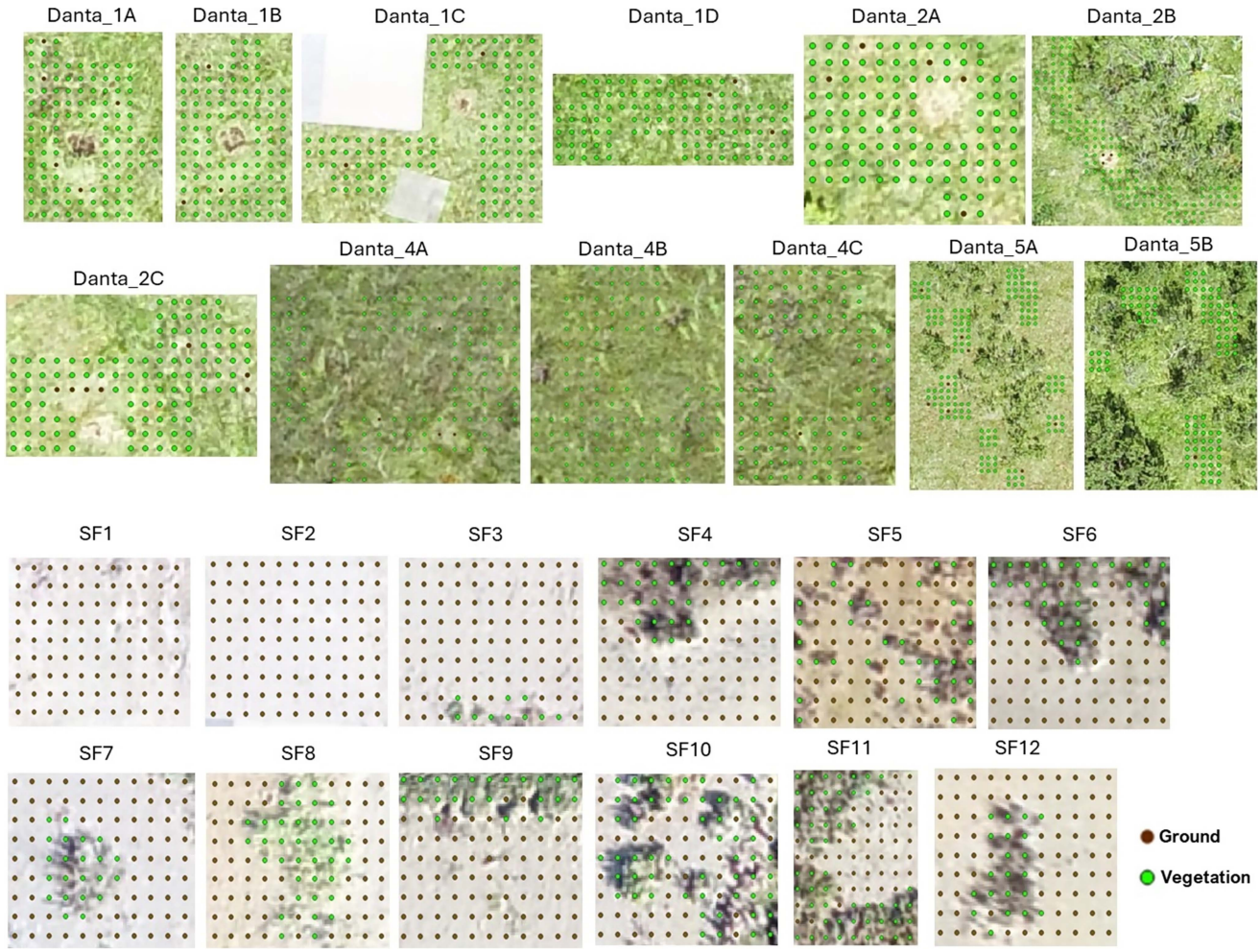

Fig. 5. Orthophoto-based percentage cover assessment in the Danta peatland and the San Felice salt marsh.

points instead of the derived dense point clouds. The concept is similar to that in [54], where airborne discrete-return LiDAR points were used instead of the full waveform to estimate height and LAI for short wetland vegetation. Primary tie points were utilized in this study since the goal was to obtain raw 3-D information comparable to LiDAR. According to [62], tie points are based on aerial triangulation and bundle block adjustment, where feature points are searched and matched across all images. Dense point clouds are based on depth maps built on the primary tie points through stereo matching. The former may not be as comprehensive as the latter concerning point density, geometry, and surface representation; however, primary tie points already have the fundamental geometric information and accuracy needed.

As mentioned in Section II, the final tie points underwent the gradual selection process to remove unreliable data points to improve data quality and accuracy. It was based on the documentation provided by Over et al. [63], which was originally developed for singular and repeat collections of nadir and near-nadir shoreline imagery that utilize the combination of camera locations and GCPs to produce DEMs and orthorectified imagery products using Agisoft Metashape Professional. Although the study areas were not within shorelines, the images were collected at nadir, and each study area has its own set of GCPs. Thus, the adaptability of the methodology was possible. Adhering to a workflow in performing noise reduction for tie points is also fundamental to ensure the replicability of this study's methodology. The documentation suggests that the gradual selection process is finished when $<10\%$ of the original tie points remain, and the final RMSE is between 0.13 and 0.18 pixels. In this study, the first criteria were achieved, but final RMSE values were not within the acceptable range (0.24 and 0.31 pixels for Danta and San Felice, respectively). According to the documentation, it is possible that the project may not support the level of error reduction if the target RMSE is not achieved. To maintain repeatability, the gradual selection process applied in this study did not deviate from the suggested default coefficient values, and only reoptimization was performed to improve the results; however, the final RMSE values were still above the target range. Therefore, it was decided to stop at the point where the first criteria were met at the highest possible RMSE to avoid the issue of overfitting. This part of the methodology could still be improved by changing the default coefficients when tested in other low-vegetation environments. Despite this limitation, the

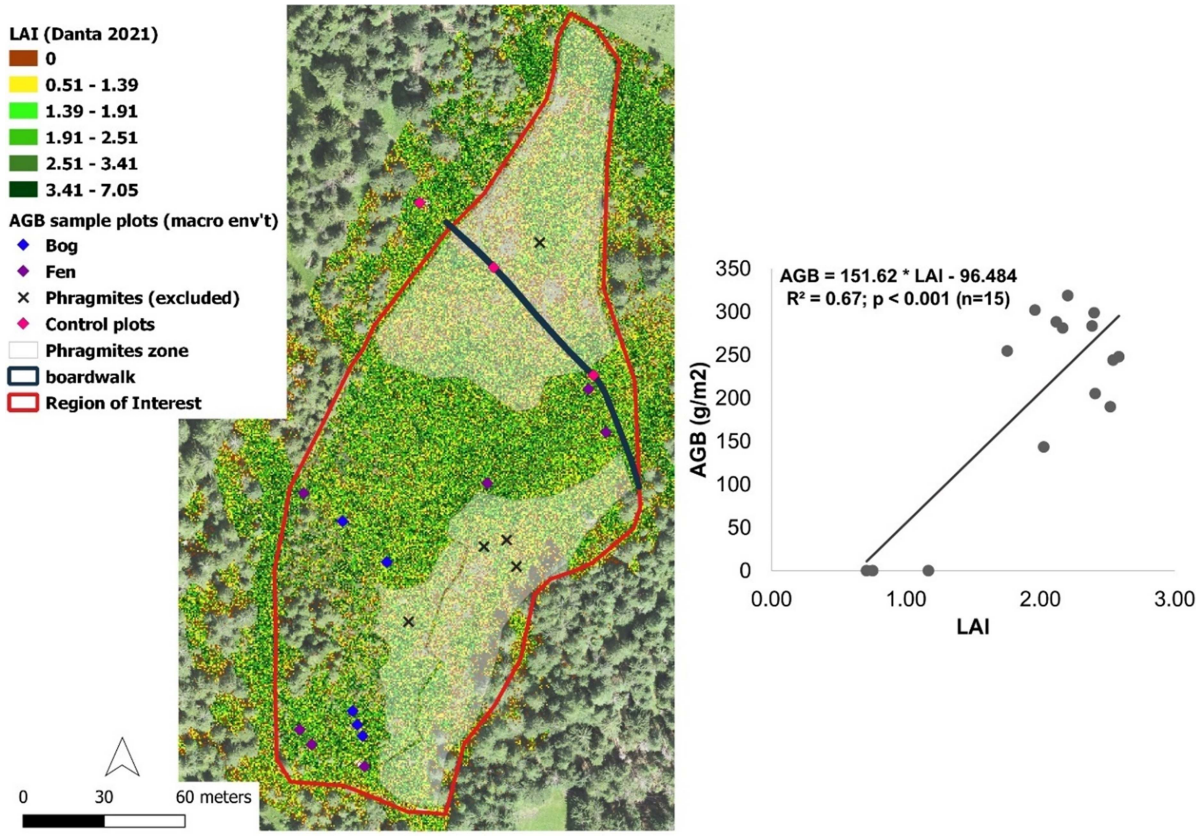

(a)

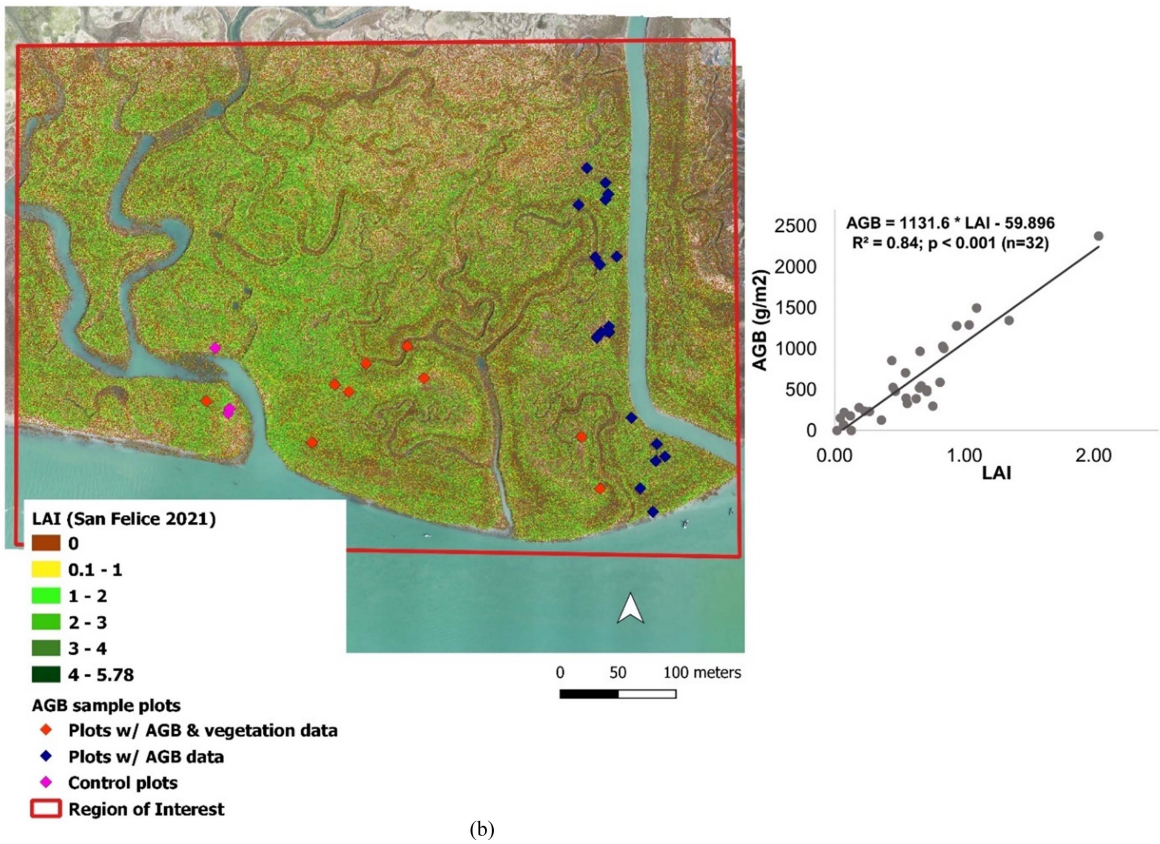

(b)

Fig. 6. LAI map and correlation with field-derived AGB for (a) Danta peatland and (b) San Felice.

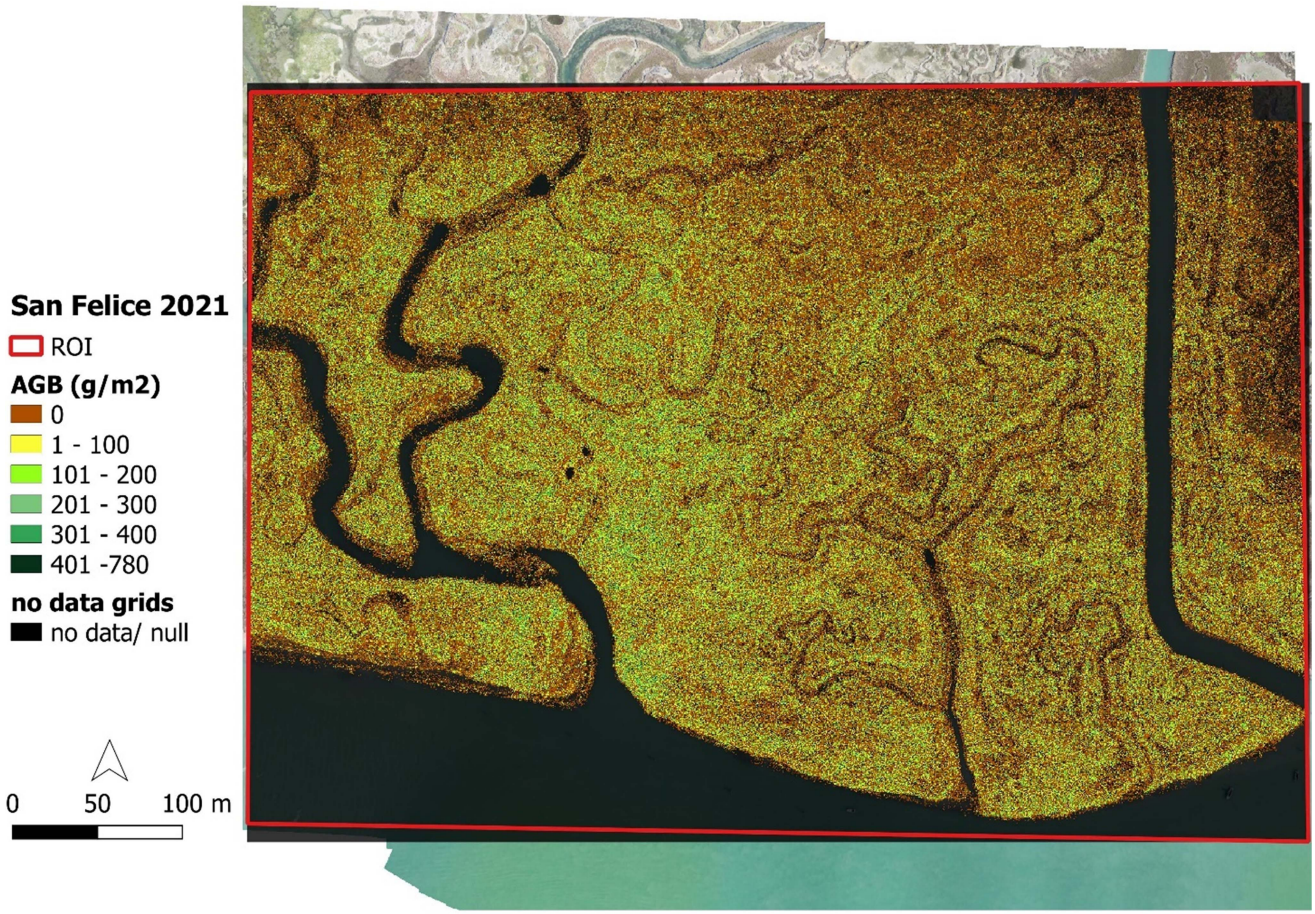

Fig. 7. Estimated AGB distribution map across the San Felice marsh for 2021 using the SfM-derived LAI and field-derived AGB correlation equation in Fig. 5.

final tie point data for both study areas were sufficient for the research objectives.

B. Ground Filtering and DTM Creation

Accurately separating LiDAR ground points from vegetation points remains a challenge, especially in wetlands [10], [54], [68]. This problem was also apparent in RGB tie point data, especially in the densely vegetated Danta peatland.

All ground filtering methods tested in this study overestimated the ground elevation. The best result was obtained by applying the PMF and then extracting the minimum height at 0.5-m grid. Previous studies [72], [73], [74] have highlighted that highly dense low vegetation causes the greatest inaccuracies in ground point detection and extraction. New approaches should be developed specifically to address this issue in wetlands, where vegetation is low and characterized by spatial variations due to the presence of numerous species, making it less homogeneous than in agricultural systems. Machine-learning-based approaches [75], [76] may offer a viable solution to this problem.

Similar to the DTM correlation result in [10], a possible datum shift between the drone and ground GPS was still apparent. This shift was not observed in the DTM correlation of San Felice; however, point misclassification might have still occurred in ground areas surrounded by vegetation based on the SE and MAE values in Table V. There might still be a need to tweak the window size and elevation thresholds in future processing to improve the ground classification result.

C. LAI Estimation and Point Density Distribution

It was evident that using RGB tie point data in estimating LAI in areas covered by tall and highly dense vegetation, such as in the case of the Phragmites portions of the Danta peatland, is ineffective compared to the result obtained in the study of Assiri et al. [10] using UAV-LiDAR data. Even with the exclusion of areas that were dominated by tall Phragmites species, the LAI–AGB correlation was still poor since the vegetation in the bogs and fen plots is very dense. Sample plots in areas with no vegetation, such as portions of the boardwalk, were also included as check plots. In these areas, LAI values of >0.5 were detected, meaning that some points were misclassified as vegetation. The difficulty in obtaining accurate ground points was also evident in the percentage cover assessment, wherein only a few ground points were identified in the sample plots in Danta, given the peatland's dense vegetation.

Pinton et al. [23] evaluated drone-based LiDAR and SfM dense point cloud data in estimating ground elevation, vegetation height, and vegetation density on a highly vegetated salt marsh.

TABLE V
DTM VALIDATION STATISTICS FOR THE (A) DANTA PEATLAND AND (B) SAN FELICE SALT MARSH

(a) Danta	R^2	Pearson's correlation coefficient	SE	MAE	Observations
Boardwalk	0.89	0.94	0.06	0.04	175
Vegetation Zone 1	0.98	0.99	0.10	0.28	45
Vegetation Zone 2	0.54	0.74	0.06	0.22	50
Vegetation Zone 3	0.78	0.88	0.07	0.17	33
Vegetation Zone 4	0.33	0.57	0.07	0.22	10
Vegetation Zone 5	0.96	0.98	0.12	0.22	34
Vegetation Zone 6	0.92	0.96	0.14	0.26	21
Vegetation Zone 7	0.98	0.99	0.06	0.23	30
(b) San Felice	R^2	**Pearson's correlation coefficient**	**SE**	**MAE**	**Observations**
Control points	0.62	0.79	0.06	0.05	18
Transect 1	0.89	0.94	0.03	0.07	10
Transect 2	0.61	0.78	0.04	0.07	9
Transect 3	0.53	0.73	0.04	0.13	8
Transect 4	0.78	0.88	0.02	0.13	8
Transect 5	0.71	0.84	0.03	0.11	10
Transect 6	0.40	0.63	0.05	0.08	8
Transect 7	0.89	0.94	0.02	0.08	6
Transect 8	0.85	0.92	0.05	0.13	8
Transect 9	0.92	0.96	0.04	0.11	6
Transect 10	0.81	0.9	0.05	0.15	9
Transect 11	0.95	0.98	0.05	0.13	7

Their study suggested that the point clouds derived from the former are more effective than the latter. This may be true in their case since the vegetation density of *Spartina alterniflora* in the U.S. is known to be very high, and tall *Spartina alterniflora* is generally more than 2 m high; hence, UAV-LiDAR is far more effective in wetlands with denser vegetation cover compared to UAV-SfM data. However, in our case, using RGB tie points was sufficient and effective in estimating LAI, given that the vegetation cover is sparser in the San Felice salt marsh, as shown in Table III.

The result also demonstrates that the parameters chosen in the LiDAR point cloud processing of [10] are also applicable to UAV-SfM tie point data.

Overall, the method in this study is sensitive to vegetation density/biomass and works well in sparser and shorter vegetation, as in the case of the salt marshes in a typical Mediterranean lagoon. The replicability can also be tested on areas with similar characteristics, such as agricultural and urban green areas. The advantage of the flexibility, quality retention, and low-cost nature of SfM has been widely demonstrated [63], [68], [77], [78], [79], and the advantage of being able to obtain UAV-SfM tie point cloud at a faster rate compared to its LiDAR counterpart should be maximized accordingly. However, the drone's flying height should be lowered to produce orthophotos with higher spatial resolution and increase the accuracy of orthophoto-based analyses.

The method used in this study, based on gap fraction probability, takes advantage of the variation in the vertical distribution of tie points to derive LAI and, subsequently, AGB. However, the core assumption of the method relies on the accuracy of the proportion between returns intercepted by the canopy and those coming from the ground. If the error predominantly affects the number of returns from the ground rather than those from the canopy, it compromises the accuracy of the method by altering the proportion between the two variables, and this may depend on both the vegetation density and the canopy structure complexity. As for salt marshes, for example, when vegetation density is low, returns can reliably reach the ground, resulting in high accuracy in determining soil elevation using both UAV-LiDAR [29] and UAV-photogrammetry from SfM techniques [55]. In fact, DTMs derived from the two methods are fully comparable [55]. When the vegetation density is higher, as in the case of peatlands, it has been observed that both technologies show limitations in reaching the soil surface [80]. Although we have not found literature indicating how the increase in complexity in the canopy structure of wetlands might have an effect similar to vegetation density, we hypothesize that this occurs especially in peatlands, where there are many shrubs and sphagnum mosses that continuously cover the soil. Further studies should explore the relationship between canopy complexity and the penetration of returns in different wetland ecosystems, particularly in peatland.

V. Conclusion

Wetlands provide a vital suite of regulating, provisioning, supporting, and cultural ecosystem services; thus, understanding their vegetation and structural attributes is important to manage these ecosystems effectively. UAV-LiDAR point cloud has been considered an effective tool for vegetation assessment in wetlands, but it can be costly. This research was able to utilize the cheaper and more rapid counterpart, UAV-SfM tie point cloud data, in LAI and AGB estimation using a workflow that was originally developed for LiDAR.

The result was unsatisfactory in densely vegetated wetlands, such as the Danta peatland; however, the method is effective in sparser and low-vegetated environments, such as the San Felice salt marsh. The flexibility and low-cost nature of UAV-SfM, and its ability to produce quality information much faster, should be further maximized in vegetation monitoring and assessment, even in other environments such as agricultural lands and urban green spaces.

Appendix

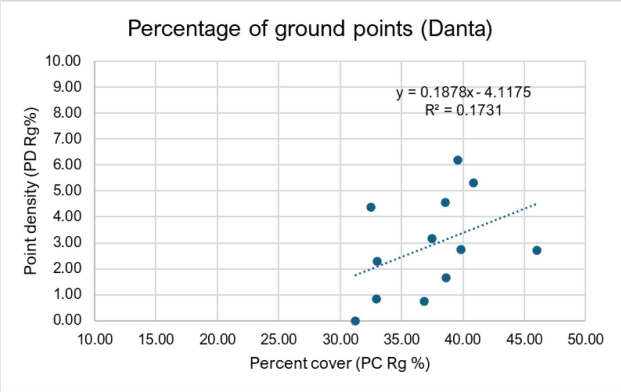

Fig. 8. Correlation between percentage cover and point density in the Danta peatland.

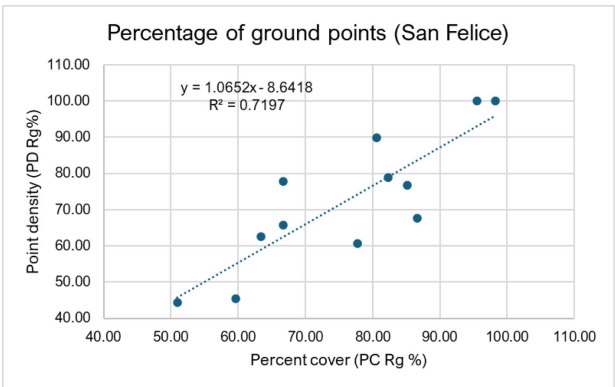

Fig. 9. Correlation between percentage cover and point density in the San Felice salt marsh.

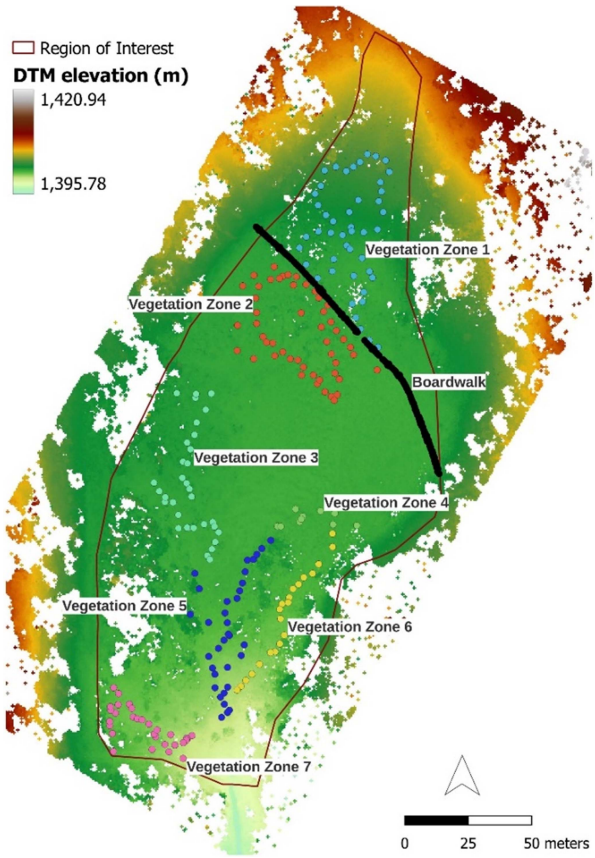

Fig. 10. DTM map of the Danta peatland with the GPS points along the boardwalk and vegetation zones.

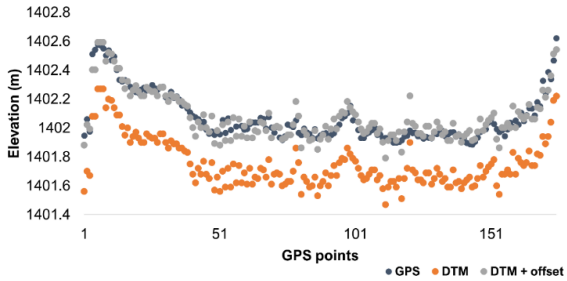

Fig. 11. Elevation value comparison (DTM versus GPS) along the boardwalk in the Danta peatland.

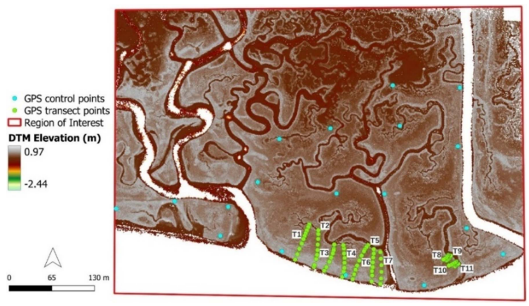

Fig. 12. DTM map of the San Felice salt marsh with the GPS location of the drone control points and sample transect points.

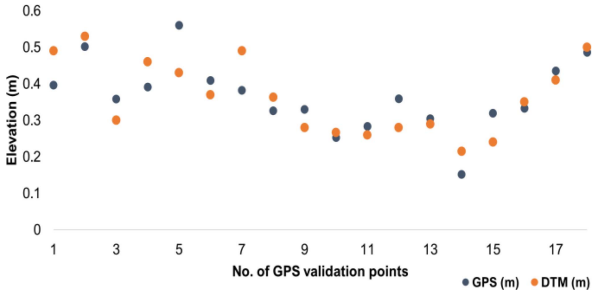

Fig. 13. Elevation value comparison (DTM versus GPS) of the 18 GCPs in the San Felice salt marsh.

ACKNOWLEDGMENT

The authors would like to acknowledge Antonio Persichetti and Cristiano Miele of Archetipo S.R.L. for providing the UAV datasets of the study sites, and Anna Sartori, Tegan Blount, Ruth Cuenca, and Olinda Rufo for having contributed to retrieving DGPS data and above-ground biomass values. The authors would also like to thank Prof. Alberto Guarnieri of the Department of Territory and Agro-Forestry Systems, University of Padova, in providing a facility for data processing.

REFERENCES

[1] H. Chen et al., "The carbon stock of alpine peatlands on the Qinghai-Tibetan Plateau during the Holocene and their future fate," *Quaternary Sci. Rev.*, vol. 95, pp. 151–158, May 2014, doi: 10.1016/j.quascirev.2014.05.003.

[2] E. Gorham, "Northern peatlands: Role in the carbon cycle and probable responses to climatic warming," *Ecol. Appl.*, vol. 1, pp. 182–195, 1991, doi: 10.2307/1941811.

[3] J. Turunen, E. Tomppo, K. Tolonen, and A. Reinikainen, "Estimating carbon accumulation rates of undrained mires in Finland application to boreal and subarctic regions," *Holocene*, vol. 12, no. 1, pp. 69–80, Jan. 2002, doi: 10.1191/0959683602hl522rp.

[4] J. Limpens et al., "Peatlands and the carbon cycle: From local processes to global implications—A synthesis," *Biogeosci. Discuss.*, vol. 5, no. 1, pp. 1379–1419, May 2008, doi: 10.5194/bg-5-1475-2008.

[5] Z. Yu, J. Loisel, D. P. Brosseau, D. W. Beilman, and S. J. Hunt, "Global peatland dynamics since the last Glacial maximum," *Geophys. Res. Lett.*, vol. 37, no. 1, Jan. 2010, Art. no. L13402, doi: 10.1029/2010GL043584.

[6] B. Minasny et al., "Digital mapping of peatlands—A critical review," *Earth-Sci. Rev.*, vol. 196, May 2019, Art. no. 102870, doi: 10.1016/j.earscirev.2019.05.014.

[7] S. Guiliani and L. Bellucci, "Salt marshes: Their role in our society and threats posed to their existence," *World Seas: Environ. Eval.*, vol. 1, pp. 79–101, Jan. 2019, doi: 10.1016/B978-0-12-805052-1.00004-8.

[8] E. B. Barbier, S. D. Hacker, C. Kennedy, E. W. Koch, A. C. Stier, and B. R. Silliman, "The value of estuarine and coastal ecosystem services," *Ecol. Monogr.*, vol. 81, no. 2, pp. 169–193, Jun. 2011, doi: 10.1890/10-1510.1.

[9] National Oceanic and Atmospheric Administration, "What is a salt marsh," Ocean Serv., 2017. [Online]. Available: https://oceanservice.noaa.gov/facts/salt-marsh.html

[10] M. Assiri et al., "Leaf area index and aboveground biomass estimation of an alpine peatland with a UAV multi-sensor approach," *GISci. Remote Sens.*, vol. 60, no. 1, Jan. 2023, Art. no. 2270791, doi: 10.1080/15481603.2023.2270791.

[11] R. Gerdol and M. Tomaselli, "Evaluation of vegetation classifications from peatlands in the Dolomites (S-Alps)," *Studia Geobotanica*, vol. 4, no. 1, pp. 25–39, Jan. 1984.

[12] R. Gerdol, M. Tomaselli, and L. Bragazza, "A floristic-ecologic classification of five mire sites in the montane subalpine belt of South Tyrol (S Alps, Italy)," *Phyton Ann. Rei Bot.*, vol. 34, no. 1, pp. 35–56, Jan. 1994.

[13] L. Bragazza, "Conservation priority of Italian Alpine habitats: A floristic approach based on potential distribution of vascular plant species," *Biodiversity Conservation*, vol. 18, no. 11, pp. 2823–2835, Nov. 2009, doi: 10.1007/s10531-009-9609-3.

[14] M. Carbognani, M. Tomaselli, and A. Pertaglia, "Interactions and covariation of ecological drivers control CO_2 fluxes in an alpine peatland," *Wetlands*, vol. 43, pp. 43–44, Jan. 2023, doi: 10.1007/s13157-023-01692-5.

[15] S. Fronzek, T. R. Carter, and K. Jyhlä, "Representing two centuries of past and future climate for assessing risks to biodiversity in Europe," *Glob. Ecol. Biogeogr.*, vol. 21, no. 1, pp. 19–35, Jan. 2012, doi: 10.1111/j.1466-8238.2011.00695.x.

[16] M. Succow and H. Joosten, *Landschaftsökologische Moorkunde*. Stuttgart, Germany: Schweizerbart'sche Verlagsbuchhandlung, 2001.

[17] M. Roner et al., "Spatial variation of salt marsh organic and inorganic deposition and organic carbon accumulation: Inferences from the Venice lagoon, Italy," *Adv. Water Resour.*, vol. 1, pp. 1–12, Nov. 2015, doi: 10.1016/j.advwatres.2015.11.011.

[18] R. Costanza et al., "The value of the world's ecosystem services and natural capital," *Nature*, vol. 387, no. 1, pp. 253–260, May 1997, doi: 10.1038/387253a0.

[19] L. G. Larsen, S. Moseman, A. E. Santoro, K. Hopfensperger, and A. Burgin, "A complex system approach to predicting effects of sea level rise and nitrogen loading on nitrogen cycling in coastal wetland ecosystem," in *Proc. Eco-DAS VIII Symp.*, 2010, pp. 67–92.

[20] S. Silvestri, A. D'Alpaos, G. Nordio, and L. Carniello, "Anthropogenic modifications can significantly influence the local mean sea level and affect the survival of salt marshes in shallow tidal systems," *J. Geophys. Res.: Earth Surf.*, vol. 123, no. 5, pp. 996–1012, May 2018, doi: 10.1029/2017JF004503.

[21] S. Silvestri, M. Marani, and A. Marani, "Hyperspectral remote sensing of salt marsh vegetation, morphology, and soil topography," *Phys. Chem. Earth A/B/C*, vol. 28, no. 1, pp. 15–25, Jan. 2003, doi: 10.1016/S1474-7065(03)00004-4.

[22] S. Silvestri, A. Defina, and M. Marani, "Tidal regime, salinity and salt marsh plant zonation," *Estuarine, Coastal Shelf Sci.*, vol. 62, no. 1, pp. 119–130, Jan. 2005, doi: 10.1016/j.ecss.2004.08.010.

[23] D. Pinton, A. Canestrelli, B. Wilkinson, P. Ifju, and A. Ortega, "Estimating ground elevation and vegetation characteristics in coastal salt marshes using UAV-based LiDAR and digital aerial photogrammetry," *Remote Sens.*, vol. 13, no. 22, Nov. 2021, Art. no. 4506, doi: 10.3390/rs13224506.

[24] P. Mao et al., "An improved approach to estimate above-ground volume and biomass of desert shrub communities based on UAV RGB images," *Ecol. Indicators*, vol. 125, Apr. 2021, Art. no. 107494, doi: 10.1016/j.ecolind.2021.107494.

[25] B. Poulter et al., "Contribution of semi-arid ecosystems to interannual variability of the global carbon cycle," *Nature*, vol. 509, no. 7502, pp. 600–603, May 2014, doi: 10.1038/nature13376.

[26] M. Xu et al., "Remote sensing-based shrub above-ground biomass and carbon storage mapping in Mu Us desert, China," *Sci. China Technol. Sci.*, vol. 53, no. 1, pp. 176–183, Jan. 2010, doi: 10.1007/s11431-010-3231-1.

[27] L. Bragazza, "Delimitation of the aerobic peat layer in a Sphagnum mire on the Southern Alps," *Oecol. Montana*, vol. 5, pp. 41–46, 1996.

[28] M. Marani, T. Zillio, E. Belluco, S. Silvestri, and A. Maritan, "Non-neutral vegetation dynamics," *PLoS One*, vol. 1, 2006, Art. no. e78, doi: 10.1371/journal.pone.0000078.

[29] T. Blount, S. Silvestri, M. Marani, and A. D'Alpaos, "LiDAR derived salt marsh topography and biomass: Defining accuracy and spatial patterns of uncertainty," *Int. Arch. Photogrammetry, Remote Sens. Spatial, Inf. Sci.*, vol. 48, pp. 57–62, 2023, doi: 10.5194/isprs-archives-XLVIII-1-W1-2023-57-2023.

[30] S. Manfreda et al., "On the use of unmanned aerial systems for environmental monitoring," *Remote Sens.*, vol. 10, no. 4, Apr. 2018, Art. no. 641, doi: 10.3390/rs10040641.

[31] L. Pàdua et al., "UAS, sensors, and data processing in agroforestry: A review towards practical applications," *Int. J. Remote Sens.*, vol. 38, no. 9/10, pp. 2349–2391, Apr. 2017, doi: 10.1080/01431161.2017.1297548.

[32] S. Czapiewski and D. Szumińska, "An overview of remote sensing data applications in Peatland research based on works from the period 2010–2021," *Land*, vol. 11, no. 1, Jan. 2021, Art. no. 24, doi: 10.3390/land11010024.

[33] A. Räsänen et al., "Peatland leaf-area index and biomass estimation with ultra-high resolution remote sensing," *GISci. Remote Sens.*, vol. 57, no. 7, pp. 943–964, Nov. 2020, doi: 10.1080/15481603.2020.1829377.

[34] J. Steenvoorden, H. Bartholomeus, and J. Limpens, "Less is more: Optimizing vegetation mapping in peatlands using unmanned aerial vehicles (UAVs)," *Int. J. Appl. Earth Observ. Geo-Inf.*, vol. 117, Feb. 2023, Art. no. 103220, doi: 10.1016/j.jag.2023.103220.

[35] J. Cao, K. Liu, L. Zhuo, L. Liu, Y. Zhu, and L. Peng, "Combining UAV-based hyperspectral and LiDAR data for mangrove species classification using the rotation forest algorithm," *Int. J. Appl. Earth Observ. Geoinf.*, vol. 102, Oct. 2021, Art. no. 102414, doi: 10.1016/j.jag.2021.102414.

[36] Y. Yang et al., "Biophysical parameters retrieval of mangrove ecosystem using 3D point cloud descriptions from UAV photographs," *Ecol. Informat.*, vol. 72, Dec. 2022, Art. no. 101845, doi: 10.1016/j.ecoinf.2022.101845.

[37] P. Tao et al., "Recognition of ecological vegetation fairy circles in intertidal salt marshes from UAV LiDAR point clouds," *Int. J. Appl. Earth Observ. Geoinf.*, vol. 114, Nov. 2022, Art. no. 103029, doi: 10.1016/j.jag.2022.103029.

[38] L. Deng et al., "Comparison of 2D and 3D vegetation species mapping in three natural scenarios using UAV-LiDAR point clouds and improved deep learning methods," *Int. J. Appl. Earth Observ. Geoinf.*, vol. 125, Dec. 2023, Art. no. 103588, doi: 10.1016/j.jag.2023.103588.

[39] J. Wijesingha, T. Moeckel, F. Hensgen, and M. Wachendorf, "Evaluation of 3D point cloud-based models for the prediction of grassland biomass," *Int. J. Appl. Earth Observ. Geoinf.*, vol. 78, pp. 352–359, 2019, doi: 10.1016/j.jag.2018.10.006.

[40] N. Lu et al., "Improved estimation of aboveground biomass in wheat from RGB imagery and point cloud data acquired with a low-cost unmanned aerial vehicle system," *Plant Methods*, vol. 15, 2019, Art. no. 17, doi: 10.1186/s13007-019-0402-3.

[41] J. ten Harkel, H. Bartholomeus, and L. Kooistra, "Biomass and crop height estimation of different crops using UAV-based LiDAR," *Remote Sens.*, vol. 12, no. 1, 2019, Art. no. 17, doi: 10.3390/rs12010017.

[42] C. J. Houldcroft, C. L. Campbell, I. J. Davenport, R. J. Gurney, and N. Holden, "Measurement of canopy geometry characteristics using lidar laser altimetry: A feasibility study," *IEEE Trans. Geosci. Remote Sens.*, vol. 43, no. 10, pp. 2270–2282, Oct. 2005, doi: 10.1109/TGRS.2005.856639.

[43] Y. Qiu, H. Duan, H. Xie, X. Ding, and Y. Jiao, "Design and development of a web-based interactive twin platform for watershed management," *Trans. GIS*, vol. 26, no. 3, pp. 1299–1317, 2022, doi: 10.1111/tgis.12904.

[44] J. Qi et al., "Applying 3D spatial metrics for landscape planning: Creating and measuring landscape scenarios by a point cloud-based approach," *Ecol. Informat.*, vol. 79, Mar. 2024, Art. no. 102436, doi: 10.1016/j.ecoinf.2023.102436.

[45] J. J. Richardson, L. M. Moskal, and S. H. Kim, "Modeling approaches to estimate effective leaf area index from aerial discrete-return LIDAR," *Agricultural Forest Meteorol.*, vol. 149, no. 6/7, pp. 1152–1160, Jun. 2009, doi: 10.1016/j.agrformet.2009.02.007.

[46] L. Qiao et al., "Improving estimation of LAI dynamic by fusion of morphological and vegetation indices based on UAV imagery," *Comput. Electron. Agriculture*, vol. 192, Jan. 2022, Art. no. 106603, doi: 10.1016/j.compag.2021.106603.

[47] A. Rasanen, J. Wagner, G. Hugelius, and T. Virtanen, "Aboveground biomass patterns across treeless Northern landscapes," *Int. J. Remote Sens.*, vol. 42, no. 12, pp. 4536–4561, 2021, doi: 10.1080/01431161.2021.1897187.

[48] J. M. Norman and G. S. Campbell, "Canopy structure," in *Plant Physiological Ecology: Field Methods and Instrumentation*. Dordrecht, The Netherlands: Springer-Verlag, 1989, pp. 301–325, doi: 10.1007/978-94-009-2221-1_14.

[49] J. M. Chen and J. Cihlar, "Quantifying the effect of canopy architecture on optical measurements of leaf area index using two gap size analysis methods," *IEEE Trans. Geosci. Remote Sens.*, vol. 33, no. 3, pp. 777–787, May 1995, doi: 10.1109/36.387593.

[50] H. Fang, F. Baret, S. Plummer, and G. Schaepman-Strub, "An overview of global leaf area index (LAI): Methods, products, validation, and applications," *Rev. Geophys.*, vol. 57, no. 3, pp. 739–799, Sep. 2019, doi: 10.1029/2018rg000608.

[51] G. Zheng and L. M. Moskal, "Retrieving leaf area index (LAI) using remote sensing: Theories, methods and sensors," *Sensors*, vol. 9, no. 4, pp. 2719–2745, Apr. 2009, doi: 10.3390/s90402719.

[52] A. Granier, D. Loustau, and N. Bréda, "A generic model of forest canopy conductance dependent on climate, soil water availability and leaf area index," *Ann. Forest Sci.*, vol. 57, no. 8, pp. 755–765, Dec. 2000.

[53] G. P. Asner, J. M. O. Scurlock, and J. A. Hicke, "Global synthesis of leaf area index observations: Implications for ecological and remote sensing studies," *Glob. Ecol. Biogeogr.*, vol. 12, no. 3 pp. 191–205, Apr. 2003, doi: 10.1046/j.1466-822X.2003.00026.x.

[54] S. Luo et al., "Estimation of wetland vegetation height and leaf area index using airborne laser scanning data," *Ecol. Indicators*, vol. 48, pp. 550–559, Nov. 2015, doi: 10.1016/j.ecolind.2014.09.024.

[55] M. Kalacska, G. Chmura, O. Lucanus, D. Bérubé, and J. Arroyo-Mora, "Structure from motion will revolutionize analyses of tidal wetland landscapes," *Remote Sens. Environ.*, vol. 199, pp. 14–24, Oct. 2017, doi: 10.1016/j.rse.2017.06.023.

[56] C. Gomez, Y. Hayakawa, and H. Obanawa, "A study of Japanese landscapes using structure from motion derived DSMs and DEMs based on historical aerial photographs: New opportunities for vegetation monitoring and diachronic geomorphology," *Geomorphology*, vol. 242, pp. 11–20, Oct. 2015, doi: 10.1016/j.geomorph.2015.02.021.

[57] S. K. Nouwakpo, M. A. Weltz, and K. McGwire, "Assessing the performance of structure-from-motion photogrammetry and terrestrial LiDAR for reconstructing soil surface microtopography of naturally vegetated plots," *Earth Surf. Process. Landforms*, vol. 41, no. 3, pp. 308–322, Mar. 2016, doi: 10.1002/esp.3787.

[58] E. Biondi et al., "Plant communities of Italy: The vegetation prodrome," *Plant Biosyst.-Int. J. Dealing Aspects Plant Biol.*, vol. 148, no. 4, pp. 728–814, Dec. 2014, doi: 10.1080/11263504.2014.948527.

[59] E. Belluco et al., "Mapping salt-marsh vegetation by multispectral and hyperspectral remote sensing," *Remote Sens. Environ.*, vol. 105, no. 1, pp. 54–67, Oct. 2006, doi: 10.1016/j.rse.2006.06.006.

[60] C. Wang, M. Menenti, M. P. Stoll, E. Belluco, and M. Marani, "Mapping mixed vegetation communities in salt marshes using airborne spectral data," *Remote Sens. Environ.*, vol. 107, no. 4, pp. 559–570, Apr. 2007, doi: 10.1016/j.rse.2006.10.007.

[61] Z. Yang, A. D'Alpaos, M. Marani, and S. Silvestri, "Assessing the fractional abundance of highly mixed salt-marsh vegetation using random forest soft classification," *Remote Sens.*, vol. 12, no. 19, Sep. 2020, Art. no. 3224, doi: 10.3390/rs12193224.

[62] L. L. C. Agisoft, *Agisoft Metashape User Manual: Professional Edition, Version 2.0*, vol. 2. St. Petersburg, Russia: Agisoft, Jun. 2023.

[63] J. R. Over et al., "Processing coastal imagery with Agisoft Metashape Professional Edition, version 1.6—Structure from motion workflow documentation," U.S. Geological Survey, Reston, VA, USA, Open-File Rep. 2021-1039, Apr. 2021, doi: 10.3133/ofr20211039.

[64] J. R. Roussel et al., "lidR: An R package for analysis of airborne laser scanning (ALS) data," *Remote Sens. Environ.*, vol. 251, Apr. 2020, Art. no. 112061, doi: 10.1016/j.rse.2020.112061.

[65] K. Zhang, S. C. Chen, D. Whitman, M. L. Shyu, J. Yan, and C. Zhang, "A progressive morphological filter for removing nonground measurements from airborne LIDAR data," *IEEE Trans. Geosci. Remote Sens.*, vol. 41, no. 4, pp. 872–882, Apr. 2003, doi: 10.1109/TGRS.2003.810682.

[66] F. Y. Lalimi, S. Silvestri, L. J. Moore, and M. Marani, "Coupled topographic and vegetation patterns in coastal dunes: Remote sensing observations and ecomorphodynamic implications," *J. Geophys. Res.: Biogeosci.*, vol. 122, no. 1, pp. 119–130, Jan. 2017, doi: 10.1002/2016JG003540.

[67] GDAL/OGR contributors, *GDAL/OGR Geospatial Data abstraction Software Library*. Beaverton, OR, USA: Open Source Geospatial Foundation, 2023.

[68] M. A. Brovelli, M. Cannata, and U. M. Longoni, "LIDAR data filtering and DTM interpolation within GRASS," *Trans. GIS*, vol. 8, no. 2, pp. 155–174, Jun. 2004, doi: 10.1111/j.1467-9671.2004.00173.x.

[69] X. Zhu, J. Liu, A. K. Skidmore, J. Premier, and M. Heurich, "A voxel matching method for effective leaf area index estimation in temperate deciduous forests from leaf-on and leaf-off airborne LiDAR data," *Remote Sens. Environ.*, vol. 240, 2020, Art. no. 111696, doi: 10.1016/j.rse.2020.111696.

[70] S. Silvestri et al., "Comment on soil salinity assessment by using near-infrared channel and vegetation soil salinity Index derived from Landsat 8 OLI data: A case study in the Tra Vinh Province, Mekong Delta, Vietnam by Kim-Anh Nguyen, Yuei-An Liou, Ha-Phuong Tran, Phi-Phung Hoang and Thanh-Hung Nguyen," *Prog. Earth Planet. Sci.*, vol. 9, pp. 1–8, 2022, doi: 10.1186/s40645-022-00490-7.

[71] R. A. Faelga, L. Cantelli, S. Silvestri, and B. M. S. Giambastiani, "Dune belt restoration effectiveness assessed by UAV topographic surveys (Northern Adriatic coast, Italy)," *Biogeosciences*, vol. 20, pp. 4841–4855, Dec. 2023, doi: 10.5194/bg-20-4841-2023.

[72] G. Sithole and G. Vosselman, "Experimental comparison of filter algorithms for bare-Earth extraction from airborne laser scanning point clouds," *ISPRS J. Photogrammetry Remote Sens.*, vol. 59, no. 1/2, pp. 85–101, 2004, doi: 10.1016/j.isprsjprs.2004.05.004.
[73] Y. Wang and H. Fang, "Estimation of LAI with the LiDAR technology: A review," *Remote Sens.*, vol. 12, no. 20, 2020, Art. no. 3457, doi: 10.3390/rs12203457.
[74] V. Moudrý, P. Klápště, M. Fogl, K. Gdulová, V. Barták, and R. Urban, "Assessment of LiDAR ground filtering algorithms for determining ground surface of non-natural terrain overgrown with forest and steppe vegetation," *Measurement*, vol. 150, Jan. 2020, Art. no. 107047, doi: 10.1016/j.measurement.2019.107047.
[75] N. Qin, W. Tan, L. Ma, D. Zhang, H. Guan, and J. Li, "Deep learning for filtering the ground from ALS point clouds: A dataset, evaluations and issues," *ISPRS J. Photogrammetry Remote Sens.*, vol. 202, pp. 246–261, Aug. 2023, doi: 10.1016/j.isprsjprs.2023.06.005.
[76] A. Nurunnabi, F. N. Teferle, J. Li, R. C. Lindenbergh, and A. Hunegnaw, "An efficient deep learning approach for ground point filtering in aerial laser scanning point clouds," in *Proc. Int. Arch. Photogrammetry, Remote Sens. Spatial Inf. Sci.*, 2021, pp. 31–38.
[77] M. R. James and S. Robson, "Straightforward reconstruction of 3D surfaces and topography with a camera—Accuracy and geoscience application," *J. Geophys. Res. Earth Surf.*, vol. 117, Jun. 2012, Art. no. F03017, doi: 10.1029/2011JF002289.
[78] M. J. Westoby, J. Brasington, N. F. Glasser, M. J. Hambrey, and J. M. Reynolds, "Structure-from-motion" photogrammetry—A low-cost, effective tool for geoscience applications," *Geomorphology*, vol. 179, pp. 300–314, Nov. 2012, doi: 10.1016/j.geomorph.2012.08.021.
[79] M. A. Fonstad, J. T. Dietrich, B. C. Courville, J. L. Jensen, and P. E. Carbonneau, "Topographic structure from motion—A new development in photogrammetric measurement," *Earth Surf. Process. Landforms*, vol. 38, no. 4, pp. 421–430, Mar. 2013, doi: 10.1002/esp.3366.
[80] J. Lovitt, M. M. Rahman, and G. J. McDermid, "Assessing the value of UAV photogrammetry for characterizing terrain in complex peatlands," *Remote Sens.*, vol. 9, no. 7, p. 715, 2017, doi: 10.3390/rs9070715.

Regine Anne Faelga received the B.S. degree in geography and the M.S. degree in environmental sciences from the University of the Philippines Diliman, Quezon City, Philippines, in 2011 and 2018, respectively, and the M.S. degree in environmental assessment and management from the University of Bologna, Ravenna, Italy, in 2022. She is currently working toward the Ph.D. degree in earth, life, and environmental sciences with the University of Bologna, Bologna, Italy.

She has been a Researcher since 2012. Her research interests include remote sensing applications in forest, riverine, coastal, and wetland environments using optical earth observation, aerial LiDAR, and UAV data.

Marco Assiri received the M.S. degree in natural sciences from the University of Bologna, Bologna, Italy, in 2019.

Between 2021 and 2022, he was a Research Fellow as part of the "CHANGED -CHAracteriziNG pEatlands from Drones" project, funded by the Department of Land, Environment and Forestry, University of Padova, Padova, Italy. He is currently a freelancer working in the field of wildlife conservation and management in Italy.

Sonia Silvestri received the M.S. degree in environmental sciences from the University Ca' Foscari, Venice, Italy, in 1997, and the Ph.D. degree in environmental system modeling (with a focus on remote sensing and ecogeomorphology of salt marsh systems) from the University of Padova, Padova, Italy, in 2001.

She is currently Associate Professor of Geomorphology with the Department of Biological, Geological and Environmental Sciences, University of Bologna, Bologna, Italy. She is an Adjunct Associate Professor with the Nicholas School of the Environment, Duke University, Durham, NC, USA. Her research interests include active and passive remote sensing applied to vegetation mapping, soil studies, hydrology, peatlands, tidal environments morphology, water quality in coastal environments, hyperspectral imagery analysis, and wetlands ecogeomorphology.

Prof. Silvestri was a recipient of the Marie Sklodowska Curie fellowship from the European Commission.